# UNDERSTANDING RARE SAFETY AND RELIABILITY EVENTS USING FORWARD-FLUX SAMPLING

Vikram Sudarshan, Warren D. Seider\*, and Amish J. Patel

Department of Chemical and Biomolecular Engineering

University of Pennsylvania

Philadelphia, PA 19104-6393

Jeffrey E. Arbogast

American Air Liquide

Newark, DE 19702

Submitted for publication to: Computers and Chemical Engineering

January 26, 2021

### **Abstract**

This paper presents improvements upon methods that explore rare process trajectories leading to rare safety and reliability events. It applies forward-flux sampling (FFS) from the family of sampling algorithms developed to discover rare molecular dynamics pathways. For a relatively simple, dynamic exothermic CSTR model with noisy feed concentration, it shows how to apply the FFS algorithm to simulate and analyze rare trajectories between high- and low-conversion steady states. First, it compares results with a less efficient brute-force (BF) method, and then with a transition-path sampling (TPS) method applied in simulation studies for an exothermic CSTR. The effects of varying key process parameters, i.e., the residence time,  $\tau$ , noise variance,  $\sigma_{\eta}^2$ , and the controller gain,  $K_C$ , which impact the rareness of an event, are investigated. Rates of rare-path transition between high- and low-conversion steady states, forward and backward, are shown to exhibit equilibrium ratios independent of  $\sigma_{\eta}^2$ , with the forward rates decreasing with  $\tau$  and  $K_C$ , and the backward rates increasing with  $K_C$ , whereas both increase with  $\sigma_{\eta}^2$ .

**Keywords:** Forward-flux Sampling, Molecular Dynamics, Residence time, Noise variance, Controller Gain

\* Corresponding author

Email address: seider@seas.upenn.edu (W.D. Seider)

© 2021. This manuscript version is made available under the CC-BY-NC-ND 4.0 license https://creativecommons.org/licenses/by-nc-nd/4.0/

#### 1. Introduction

Safety and reliability events are of primary concern in the process and manufacturing industries, where safety issues can cause pernicious impacts on human health and environment due to extreme operating conditions, such as high temperatures and pressures and the presence of hazardous chemicals and materials. Fortunately, it is possible to mitigate these risks.

Near the vicinities of unsafe operation, it is imperative to utilize automated safety interlocks, which have the capability to shutdown plants, thereby avoiding the related consequences. These measures, however, can increase unreliability with production-time losses due to shutdowns, maintenance, and start-up delays. Moreover, they may disrupt routine procedures, adversely impacting human health and the environment. Hence, there is a strong motivation to develop strategies to avert more effectively unsafe operations.

Alarm management schemes are a key to ensure the safety and reliability of manufacturing plants and processes. They aid in mitigating losses by ensuring that the concerned process variables remain within bounds of safe operation by triggering actionable alarms when these variables individually approach the vicinities of unsafe regions, following which, adequate steps can be taken through intervention by the operator (Mehta and Reddy, 2015). Such alarm schemes prove to be effective in tackling commonly occurring 'postulated' events that lead to interlock activation, but often fail to predict the rare 'unpostulated' event trajectories that result in abnormal events. Hence, the design of alarms based upon the detection of such rare, un-postulated event trajectories, is beneficial to ensure plant safety and reliability (Moskowitz et al., 2018).

This paper introduces two methods to detect the pathways leading to rare, un-postulated events: (1) an illustrative but inefficient brute-force (BF) method, and (2) a forward-flux sampling (FFS) method that is capable of estimating rates of rare-events. The latter is shown to trace pathways to rare events, triggering alarms that enable immediate operator interventions. The FFS method is an alternative to the transition-path sampling (TPS) method, whose application was discussed and applied by Moskowitz et al. (2018) for operation of a CSTR with an exothermic R→P reaction and an air-separation system to produce oxygen, nitrogen, and argon. Both FFS and TPS methods have been employed routinely in molecular dynamics (MD) simulations to locate rare events in stochastic non-equilibrium systems (Allen et al., 2006), including nucleation rates of hard spheres (Filion et al., 2010), methane hydrate nucleation (Bi and Li, 2014) and homogeneous nucleation of sodium chloride crystals (Jiang et al., 2018). To our knowledge, this is the first application of the FFS method for detecting rare-event pathways in process operations. Herein, the analysis of rare-event pathways by the BF and FFS methods is demonstrated using a CSTR with noisy feed concentration to carry out an exothermic R→P reaction, thereby facilitating inter-basin transition(s) between the high conversion-high temperature basin 'A' and low conversion-low temperature basin 'B'. This analysis consists of studying the effects observed

by varying key process parameters; i.e. the residence time,  $\tau$ , and the noise variance,  $\sigma_{\eta}^2$ , and are hence instrumental in dictating the rarity of a particular process trajectory. This analysis using BF and FFS methods is conducted for two process configurations for the exothermic CSTR – one without a control system and another inclusive of proportional P-control, where a third process parameter – the controller gain,  $K_{\rm C}$ , becomes critical in estimating the rarity of a particular event. Lastly, a dynamic analysis is conducted for long process trajectories near the vicinity of the transition to investigate their cause and study how the key process variables, such as the process temperature and the outlet concentration, respond to the changes caused by the noise, where it is observed that the process temperature responds first to the noise.

### 2. Description of the Exothermic CSTR

Consider a jacketed exothermic CSTR model with reaction:

$$R \rightarrow P$$
 (1)

Figure 1 shows a schematic of the model. The feed temperature and inlet concentration of A are  $T_{\rm f}$ ,  $C_{\rm Af}$  and the outlet temperature and concentration; i.e., T,  $C_{\rm A}$ , are computed to be functions of time. The model is simplified by assuming ideal mixing, completely back-mixed, with a constant residence time, and incompressible flow. The cooling water-jacket is assumed to be sufficiently large such that the cooling water temperature,  $T_{\rm C}$ , changes negligibly (for the uncontrolled process). The model also includes a temperature controller (TC) that controls T by manipulating the inlet cooling water flow-rate,  $F_{\rm C}$ . The kinetics of the reaction are elementary with the intrinsic rate of reaction:

$$-r = k_0 \exp\left(-\frac{E}{RT}\right) C_{\rm A} \tag{2}$$

where  $k_0$  is the Arrhenius pre-exponential factor, E is the activation energy, and R is the universal gas constant.

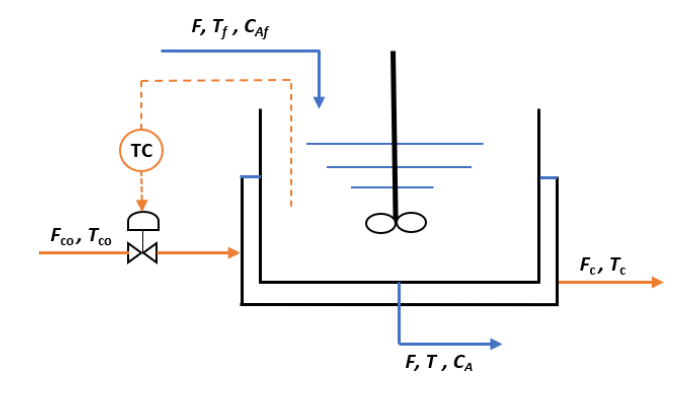


Figure 1. Schematic of the exothermic CSTR

The governing mass and energy balance equations for the uncontrolled process are:

$$V\frac{dc_{A}}{dt} = \frac{V}{\tau}(C_{Af} - C_{A}) - Vk_{0} \exp\left(-\frac{E}{RT}\right)C_{A}$$
(3)

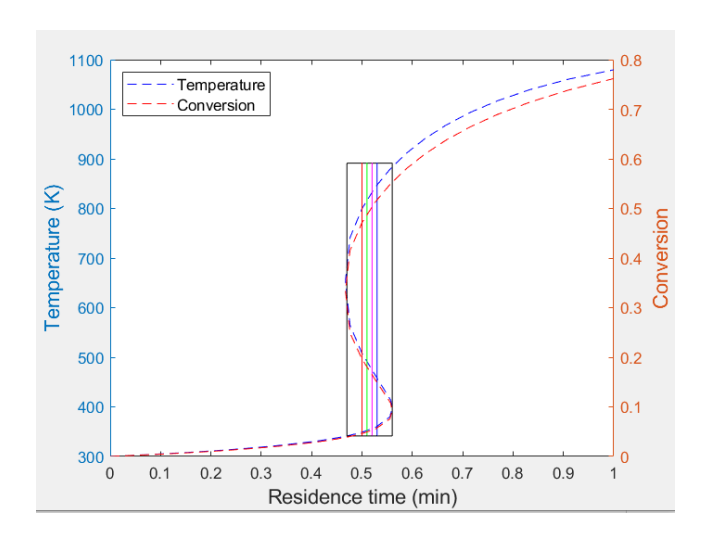
$$\rho V C_{\rm p} \frac{dT}{dt} = \frac{\rho V C_{\rm p}}{\tau} (T_{\rm f} - T) - V \Delta H k_0 \exp\left(-\frac{E}{RT}\right) C_{\rm A} + U A (T_{\rm c} - T)$$
(4)

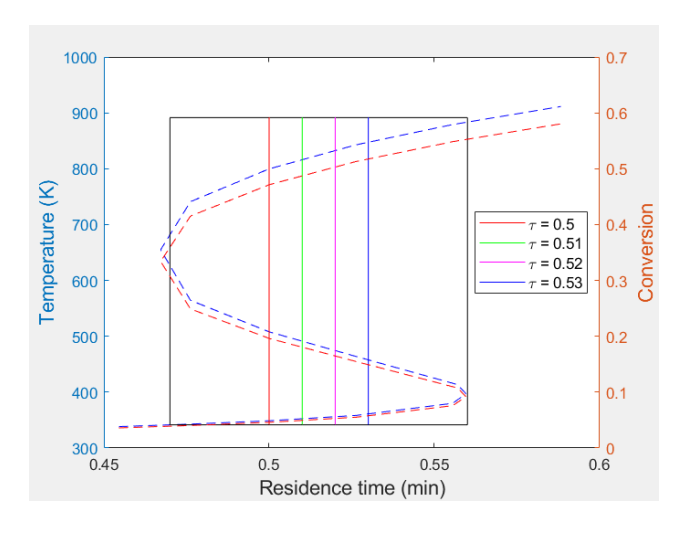
where V is the reactor volume,  $\tau$  is the residence time, U is the overall heat-transfer coefficient, A is the heat-transfer area,  $\Delta H$  is the heat of reaction,  $\rho$  is the feed density, and  $C_p$  is the heat capacity of the feed stream. Table 1 contains the constants and parameters utilized in this study.

Table 1. Process Constants and Parameters

Parameter	Value	Unit
A	30	m <sup>2</sup>
$C_{ m Af}$	2	kmol/m³
$C_{\rm p} = C_{\rm pw}$	4	kJ/(kg-K)
E	1.50E+04	kJ/kmol
$F_{\rm C0}$	30	m³/min
$k_0$	17.038	1/min
R	8.314	kJ/(kmol-K)
$T_{ m co}$	300	K
$T_{ m f}$	300	K
$T_{ m SP}$	800	K
U	100	kJ/(min-K-m <sup>2</sup> )
$V = V_{\rm j}$	10	m <sup>3</sup>
$\Delta H$	-2.20E+06	kJ/kmol
$\rho = \rho_{\rm w}$	1,000	kg/m³

Eqs. (3) and (4) are solved simultaneously to determine steady-state values for the outlet concentration and outlet temperature. This procedure is repeated for residence times ranging from  $\tau = 0$  to  $\tau = 1$  minutes, with multiple steady states detected for  $\tau = 0.47$ -0.56 min, with stable steady states at the high conversion-high temperature basin 'A' and low conversion-low temperature basin 'B' (Balakotaiah & Luss, 1983). The state variables; i.e., the conversion and outlet temperature, are shown as functions of residence time, in familiar S-shaped curves, in Figure 2a, with the black rectangle signifying the range of residence times for which multiple steady states are detected. Figure 2b shows the magnified view of the same, with colored solid lines depicting the residence times considered for analysis.





- (a) State variables as functions of residence time at steady state
- (b) Magnified view of the rectangle showing the range of  $\tau$  for which multiple steady states are detected

Figure 2. State variables as functions of residence time at steady state and magnified view of the rectangle showing the multiple steady-state range of  $\tau$ 

To facilitate inter-basin transitions, random, non-parametric noise,  $\eta$ , is added to the inlet concentration. This noise variable is sampled from a Gaussian distribution having mean,  $\mu = 0$ , and variance,  $\sigma_{\eta}^2$ . Note that the noise is sampled at every integration time-step (h = 0.01 min) and scaled appropriately. The dynamic integrations are conducted using the explicit-Euler method within acceptable bounds of numerical stability and accuracy. With noise, the governing equations are:

$$V\frac{dC_{A}}{dt} = \frac{V}{\tau}(C_{Af} + \eta - C_{A}) - Vk_{0} \exp\left(-\frac{E}{RT}\right)C_{A}$$
 (5)

$$\rho V C_{\rm p} \frac{dT}{dt} = \frac{\rho V C_{\rm p}}{\tau} (T_{\rm f} - T) - V \Delta H k_0 \exp\left(-\frac{E}{RT}\right) C_{\rm A} + U A (T_{\rm c} - T)$$
 (6)

Next, using proportional P-control to regulate the reactor temperature, T, by manipulating the cooling water flow rate,  $F_C$ , in a jacket, three controller gains are considered;  $K_C = 0.02$ , 0.05, and 0.1. The governing equations that model the P-controlled process are:

$$V\frac{dC_{A}}{dt} = \frac{V}{\tau} (C_{Af} - C_{A} + \eta) - Vk_{0} \exp\left(-\frac{E}{RT}\right) C_{A}$$
 (7)

$$\rho V C_{\rm p} \frac{dT}{dt} = \frac{\rho V C_{\rm p}}{\tau} (T_{\rm f} - T) - V \Delta H k_0 \exp\left(-\frac{E}{RT}\right) C_{\rm A} + U A (T_{\rm c} - T)$$
 (8)

$$\frac{dT_{\rm C}}{dt} = \frac{F_{\rm C}}{V_{\rm i}} (T_{\rm C0} - T_{\rm C}) - \frac{UA}{\rho_{\rm w} V_{\rm i} C_{\rm pw}} (T_{\rm C} - T)$$
(9)

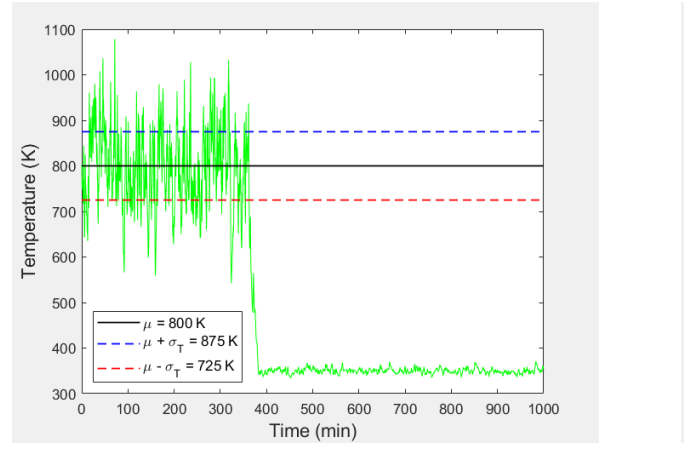
$$F_{\rm C} = F_{\rm C0} + K_{\rm C} (T - T_{\rm SP}) \tag{10}$$

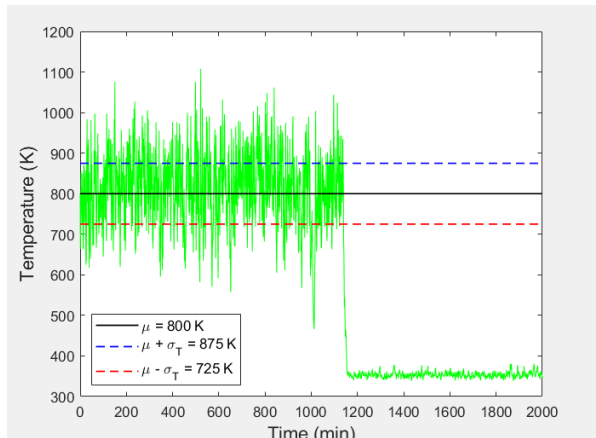
© 2021. This manuscript version is made available under the CC-BY-NC-ND 4.0 license https://creativecommons.org/licenses/by-nc-nd/4.0/

where  $F_{C0}$  is the cooling water flow rate at steady state,  $K_C$  is the controller gain,  $T_{C0}$  is the inlet temperature of the cooling water,  $T_{SP}$  is the set-point temperature for the controller,  $V_j$  is the volume of the cooling-water jacket,  $\rho_w$  is the density of the cooling water, and  $c_{pw}$  is the specific-heat capacity of the cooling water (refer to Table 1 above). Note that  $T_{SP}$  is maintained constant throughout, regardless of trajectories initiating in either basin.

Figures 3a,b show the temperature profiles for two typical dynamic trajectories for  $\sigma_{\eta}^{2} = 0.02$ , for the uncontrolled process. The time spent by the process trajectory in basin A increases with  $\tau$  for fixed  $\sigma_{\eta}^{2}$ ; i.e., it becomes more difficult for the process to transition out of basin A, but the time taken to transition from basin A to basin B,  $t_{AB}$ , is found to be independent of  $\tau$ , with  $t_{AB} = 13$  min. Note that before conducting the analyses using BF and FFS methods, the lower-bound temperature for basin A, i.e., the minimum temperature required for the process to be in basin A, needs to be estimated. As a first approximation, this lower-bound temperature is adjusted iteratively to center the distribution of temperatures attained in basin A over multiple trajectories at 800 K, thereby generating a mean,  $\mu \sim 800$  K, and the standard deviation,  $\sigma_{T} \sim 75$  K. Note that the same lower bound is used for all considered values of  $\tau$  and  $\sigma_{\eta}^{2}$ . Multiplying by two, using a heuristic, the lower bound temperature for basin A is adjusted to:

Lower bound for basin A = 
$$\mu - (2\sigma_T) \sim 650 K$$
 (11)





(a)  $\tau = 0.5 \text{ min}, \sigma_{\eta}^2 = 0.02$ 

(b)  $\tau = 0.51 \text{ min}, \sigma_n^2 = 0.02$ 

Figure 3. Temperature profiles for dynamic trajectories with noise added to inlet concentration, showing the mean,  $\mu \sim 800$  K, and the standard deviation,  $\sigma_T \sim 75$  K

### 3. Brute-force (BF) Method

Example applications for the BF method include simulation of homogeneous nucleation during the condensation of supersaturated vapors of methane, ethane, and carbon dioxide (Horsch et al., 2008), and an investigation of the association of methane in water (Zhang and McCammon, 2003).

Consider the BF method for simulation of the exothermic CSTR, which is used to compute the rate of transition from basin A to basin B as the rate of exponential decay of the survival probability of the process to remain in basin A, for rare events. The survival probability, in general, is defined as the probability of the process remaining (or 'surviving') in a particular basin (A or B) over a continuous time interval. Note that survival probabilities have been routinely studied in various domains, such as in the analysis of stochastic non-equilibrium systems with absorbing states (Muñoz et al., 1997), and to investigate the loop-closure kinetics of penta- and octa-peptides Cys-(Ala-Gly-Gln)<sub>n</sub> -Trp (n = 1 and 2) (Yeh and Hummer, 2002).

Therefore, assuming that the inter-basin transition follows first-order kinetics, the survival probability within basin A,  $p_A(t)$ , is:

$$p_{A}(t) = exp(-k^{BF}t) \tag{12}$$

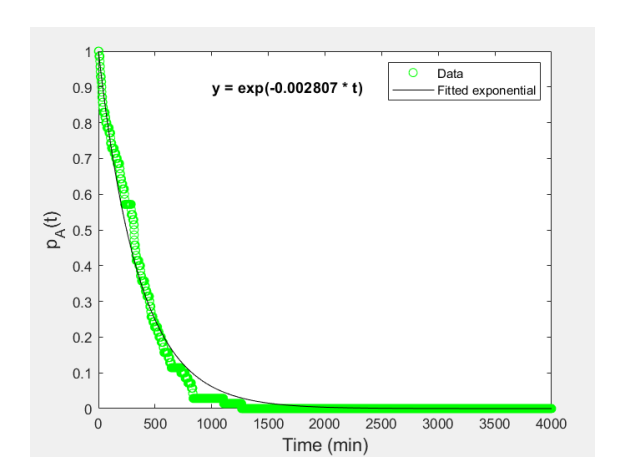
where  $k^{\rm BF}$  is the BF rate of transition. Herein, to determine k, at each residence time, ~100 trajectories are generated that trace the transition from basin A to B. To achieve this, several steps are followed:

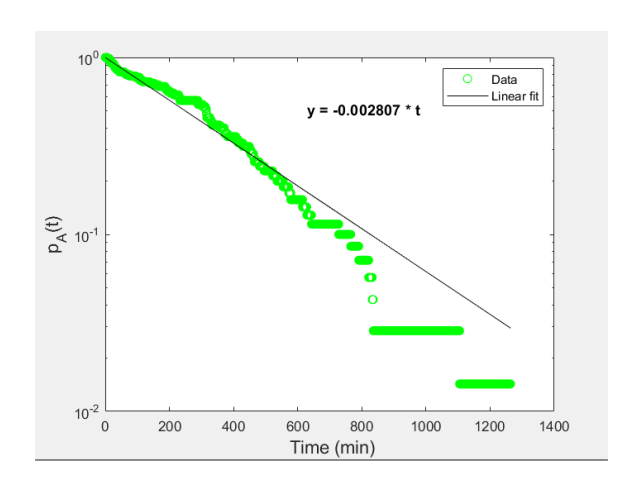
- 1) To calculate the survival probability for the reactor to remain in basin A, two main conditions are checked to conclude it has descended to basin B:
  - i) A base temperature,  $\sim 500$  K, is set below which the reactor can be considered to have descended to basin B.
  - ii) A retention time,  $\sim 2t_{AB}$ , is identified beyond which the reactor lies below 500 K. This condition is more important and critical than condition i.
- 2) For each of 100 trajectories, the survival probabilities are calculated along the dynamic profile. Then average probabilities are computed along the dynamic profiles, and, by regression, the BF rate of transition; i.e.,  $k^{BF}$  in Eq. (12), is determined.
- 3) Next, the average survival time of the reactor in basin A,  $\bar{t}_A$ , is computed:

$$\overline{t_A} = \frac{1}{k^{\text{BF}}} \tag{13}$$

Like the survival probability, the average survival time,  $\bar{t_A}$ , is defined as the average time during which the reactor remains or 'survives' in basin A before transitioning to basin B. For instance, it

can be seen in Figure 3a, for  $\tau=0.5$  min, the survival time for this process trajectory is ~ 350 min, with  $\overline{t_A}$  being the average survival time for the 100 trajectories. Figures 4a,b show an example of how the rate of transition is computed using the BF algorithm for a specific process configuration of  $\tau=0.5$  min and  $\sigma_{\eta}^{\ 2}=0.02$ , computed over 100 trajectories, on linear and semi-log scales. It can be seen here that the data validates the first-order kinetics for the transition that was assumed in Eq. (12). The linear fit showed in Figure 4b appears to decrease in accuracy with time due to the small probabilities computed at higher times.





(a) Survival probability,  $p_A(t)$  on linear scale

(b)  $p_A(t)$  on semi-log scale

Figure 4. Example of a BF simulation showing  $p_A(t)$  on linear and semi-log scales at  $\tau = 0.5$  min and  $\sigma_{\eta}^2 = 0.02$ 

Note that for the purpose of conducting the BF methods for rare events, multiple trajectories are required to be simulated. For not so rare events; i.e., for cases where multiple inter-basin back-and-forth transitions are observed, the same BF method can be applied for a long, single trajectory. Figure 5 shows an example of one such trajectory for the uncontrolled exothermic CSTR process at  $\tau = 0.53$  min and  $\sigma_n^2 = 0.2$ .

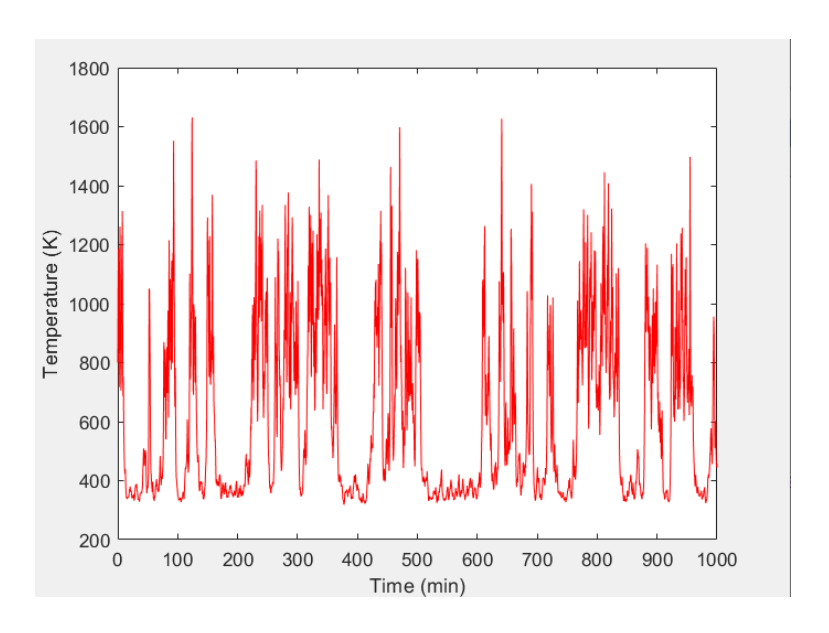


Figure 5. Long trajectory showing multiple back-and-forth, inter-basin transitions at  $\tau = 0.53$  min and  $\sigma_{\eta}^2 = 0.2$ 

The survival probability, p(t), is defined as the probability that a trajectory in a basin, initially at time  $t_0$ , remains continuously in that basin (i.e., 'survives' in the basin) over the interval  $[t_0, t_0 + t]$ . To obtain p(t), this analysis is conducted for various intervals along a single trajectory at a given t by varying  $t_0$  from  $t_0 = 0$  to  $t_0 = t_{\text{sim}} - t$ , where  $t_{\text{sim}}$  is the simulation duration of the trajectory. In this way, p(t) is computed for a particular t as the number of intervals that successfully survive in the basin, divided by the total number of intervals. For instance, the trajectory shown in Figure 5 has  $t_{\text{sim}} = 1000$  min. At t = 20 min, the various intervals for which the survival probability analysis is conducted in a basin proceed as [0, 20], [0.01, 20.01], [0.02, 20.02], ..., [979.99, 999.99], [980, 1000]; i.e,  $\sim 98,000$  intervals. Amongst these intervals, only  $N_t$  begin in basin A. Of these, there are  $n_t$  intervals that successfully survive throughout, over t = 20 min, in basin A. Hence, the survival probability at t = 20 min is computed as  $n_t/N_t$ . This analysis is conducted at all times, t, in a practical range; e.g., from t = 0.01 to  $\sim 65$  min for basin A – until the survival probability approaches zero. For basin B, however, an identical analysis is carried with all intervals beginning in basin B and successfully surviving in basin B.

### 4. Forward-Flux Sampling (FFS) Method

FFS has been utilized by the MD community to reduce the computational time and effort required to simulate rare molecular events, where the initiation times are greater than the event times by orders of magnitude; e.g., in the dissociation of a weak acid, where the initiation time (i.e., the frequency with which dissociation occurs – once per millisecond) is much greater than the 1-nanosecond dissociation time-scale (Bolhuis et al., 2002) Consequently, to counter this, FFS simulates process trajectories in a © 2021. This manuscript version is made available under the CC-BY-NC-ND 4.0 license <a href="https://creativecommons.org/licenses/by-nc-nd/4.0/">https://creativecommons.org/licenses/by-nc-nd/4.0/</a>

piecewise manner, between initial and final basins, using evenly-spaced interfaces, positioned at order parameters,  $\lambda_i$ , i = 1, ..., n-1. The initial basin (i.e., basin A) is bounded by  $\lambda_0$  and the final basin (i.e., basin B) is bounded by  $\lambda_n$ , with the intermediate interfaces bounding the intermediate basins (Allen et al., 2009). Various FFS variants have been developed; such as the branched-growth (BG) method the Rosenbluth (RB) method, and the pruning method, to name a few (Allen et al., 2006). The specific variant applied herein is the classical Direct Forward-Flux Sampling (DFFS) technique, shown schematically in Figure 6.

For this analysis, the order parameter,  $\lambda$ , is the reactor temperature, T. For each residence time, the steps involved (illustrated for the CSTR with the exothermic reaction R $\rightarrow$ P) are:

1) Generate a long, initial trajectory of the process from a starting point lying in basin A. Because it was decided that the lower bound of basin A,  $\sim 650$  K, the starting point for this initial trajectory was chosen to be 660 K. The FFS method requires a simulation time,  $t_{\text{sim}}$  ( $\sim \overline{t_A}$ ), to be selected for the long, initial trajectory.

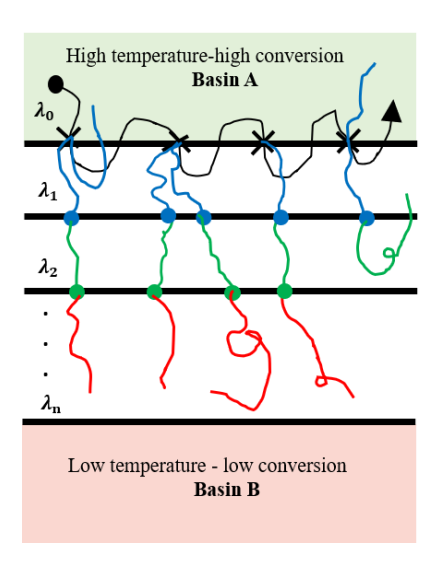


Figure 6. DFFS schematic

- 2) Compute the number of initial crossings,  $N_0$ , as the number of times this long trajectory, having simulation time  $t_{\text{sim}}$ , crosses the zeroth order parameter,  $\lambda_0 = 650 \text{ K}$ . Save T and  $C_A$  at every crossing point.
- 3) Repeat step 2 for multiple trajectories to generate a sufficient number of crossings, typically ~100 crossings. In this case, ~10 trajectories are considered, giving ~  $N_0 = 100$  initial crossings.
- 4) Calculate the initial rate of transition across  $\lambda_0$ ,  $r_1$ :

$$r_1 = \frac{\sum_{i=1}^{10} N_0^{(i)}}{\sum_{i=1}^{10} t_A^{(i)}} \tag{14}$$

where  $N_0^{(i)}$  is the initial crossings generated for trajectory i and  $t_A^{(i)}$  is the time spent by trajectory i in basin A. This approach, not only ensures a sufficient number of crossings, but generalizes as  $r_1$  represents an average computed over 10 trajectories.

- Next, to calculate the probability of transitioning from one order parameter to another, the number of interfaces and the interface spacing is chosen. The interface spacing is chosen to be 70 K (typically close to the standard deviation,  $\sigma_T$ , computed for basin A, which is 75 K), and consequently, the number of interfaces from basin A to basin B =  $N_{\text{interface}} = 4$ . Based on this, the transitioning from basin A to basin B is in 70 K increments from 650 K to 370 K (which lies within basin B), with order parameter values: (i)  $\lambda_0 = 650$  K, (ii)  $\lambda_1 = 580$  K, (iii)  $\lambda_2 = 510$  K, (iv)  $\lambda_3 = 440$  K, (v)  $\lambda_4 = 370$  K.
- 6) A random crossing point is chosen from the saved crossings as the initial point, and a trajectory is initiated from this point. This trajectory is terminated when  $\lambda_1$  has been crossed, with the crossing point values saved. It is important to efficiently select the length for this trajectory, which is:

Length of each trajectory = 
$$3 \times \frac{t_{AB}}{N_{\text{interface}}}$$
 (15)

where  $t_{AB}$  = transition time = 13 min and  $N_{interface}$  = number of interfaces = 4. The heuristic factor 3 provides sufficient time for the trajectories to transition from  $\lambda_i$  to  $\lambda_{i+1}$ .

7) Repeat step 6 for  $N(\sim N_0)$  trajectories and calculate the probability of transition over  $\lambda_1$ :

$$p_1 = \frac{N_1}{N} \tag{16}$$

where  $N_1$  is the number of trajectories, out of N, which are successful in crossing  $\lambda_1$ .

- 8) Repeat steps 6 and 7 for each order parameter,  $\lambda_i$ , to the last order parameter,  $\lambda_n$ . In this case,  $\lambda_n = \lambda_4$ .
- 9) The overall probability of transition is the product of all the probabilities of local transition computed:

Overall probability of transition = 
$$p_{\text{overall}} = \prod_{i=1}^{4} p_i$$
 (17)

10) The overall rate of transition from basin A to B is:

Overall rate of transition = 
$$k^{FFS} = r_1 \times p_{\text{overall}}$$
 (18)

Table 2 summarizes the key steps in the FFS algorithm. Note that this method is conducted in the same manner for all  $\sigma_{\eta}^2$  (including higher  $\sigma_{\eta}^2$  values, as seen in Figure 5), tracking the forward and backward transitions – for backward transitions, the starting point is in the B basin and the direction of transition is reversed (i.e., with temperature increases from  $\lambda_0 = 370$  K to  $\lambda_4 = 650$  K). The *n* values of  $p_i$ ; i.e., the local probability of transition across interface,  $\lambda_i$ , is used to calculate commitment probabilities at different points within the transition landscape. The committers show the likelihood of interlock activation increasing as the process moves away from normal operation towards the B basin. Committers are used to improve alarms by indicating the temperatures (and other variable values) along the transition landscape as probabilities of reaching basin B approach 100%, with high rates,  $r_i$ . Also, under these conditions, a switch to a more rigorous model can be achieved; e.g., involving a residence-time distribution.

Table 2. Summary of Steps in the FFS Algorithm

- 1. Generate a long, initial trajectory starting in the A basin to generate initial crossings of  $\lambda_0$ .
- 2. Record the number of initial crossings,  $N_0$ . Save T and  $C_A$  at every crossing.
- 3. Repeat step 2 for multiple trajectories to generate a sufficient number of initial crossings.
- 4. Compute the initial rate of transition across  $\lambda_0$ ,  $r_1$ , by dividing the total number of initial crossings,  $\sum N_0^{(i)}$ , by the total time spent by each trajectory i in basin A,  $\sum t_A^{(i)}$ .
- 5. Position the order parameters,  $\lambda_1, ..., \lambda_n$
- 6. Choose random crossing points from among the saved crossings and generate a trajectory which continues until  $\lambda_1$  is crossed. Save the T and  $C_A$  at this crossing.
- 7. Repeat step 6 for  $N (\sim N_0)$  trajectories
- 8. Repeat steps 6-7 at each  $\lambda_i$  until  $\lambda_n$  is reached.
- 9. Compute the overall probability of transitioning from A to B,  $p_{\text{overall}}$ , by taking the product of the probabilities for each  $\lambda_i \rightarrow \lambda_{i+1}$  transition.
- 10. Compute the overall rate of transition as the product of the overall probability,  $p_{\text{overall}}$ , and the initial rate of transition,  $r_1$ .

#### 5. Results and Discussion

Consider the rare-event analyses by the BF and FFS methods for two classes of data-sets with:

- i. Noise variance fixed at  $\sigma_n^2 = 0.02$ , and the residence time varied over  $\tau = 0.5$ -0.53 min, and
- ii. Residence time fixed at  $\tau = 0.53$  min and the noise variance increased over  $\sigma_n^2 = 0.04\text{-}0.2$ .

These data-sets have been chosen to investigate the variation of the transition rates and their related variables with both a key process variable, residence time, and the noise variance, which together dictate the rarity of each trajectory.

Furthermore, as mentioned previously, for this rare-event analysis, two process configurations are considered involving an:

- i. Uncontrolled exothermic CSTR process,
- ii. Exothermic CSTR process with proportional (P) control

### 5.1. Process Analysis Without Control

For the uncontrolled process, just the dynamic mass and energy balances, Eqs. (5) and (6), with stochastic noise,  $\eta$ , added to  $C_{Af}$ , are integrated using the explicit-Euler method, having step-size, h = 0.01 min. Multiple trajectories are generated using the BF and FFS methods to compute the rates of transition between the A and B basins.

# 5.1.1. Noise Variance Fixed at $\sigma_{\eta}^2 = 0.02$ , Vary $\tau$

Initially, the BF and FFS methods are carried out for the uncontrolled process with  $\sigma_{\eta}^{\ 2} = 0.02$ , as  $\tau$  is varied from 0.5-0.53 min. Figure 7 shows the average survival probability,  $p_{\rm A}(t)$ , as a function of time t, on a semi-log scale, for residence times  $\tau = 0.5, 0.51$ , and 0.52 min, computed using the BF algorithm. Each trajectory experiences a typical exponential decay (on a linear scale), with the magnitude of the exponential argument,  $k^{\rm BF}$ , being the BF rate of transition from basin A to basin B. It is observed that as  $\tau$  increases,  $k^{\rm BF}$  decreases because the reactor spends more time in basin A. In other words, the increase in  $\tau$  causes an increase in the average survival time,  $\bar{t}_{\rm A}$ , increasing the stability of the process in basin A. Note that, due to excessive computation times, BF analysis could not be conducted at  $\tau = 0.53$  min and  $\sigma_{\eta}^{\ 2} = 0.02$ .

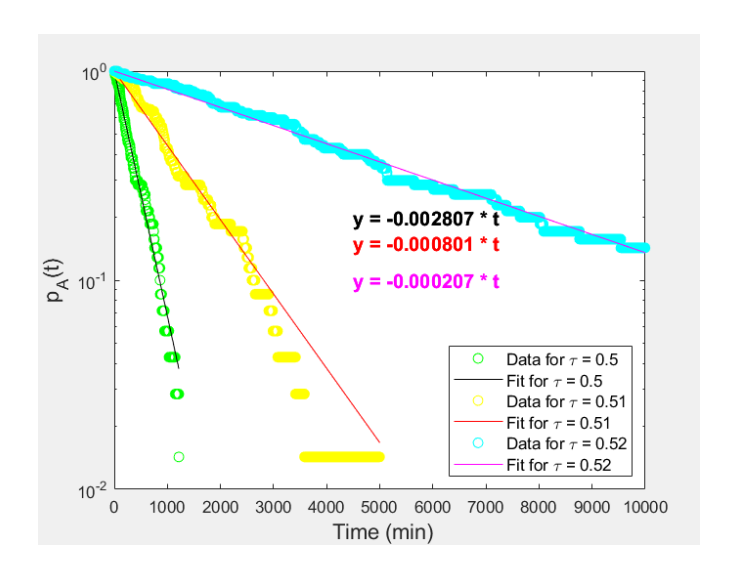


Figure 7. Average survival probability in basin A,  $p_A(t)$ , on a semi-log scale for three residence times, computed by BF algorithm

Similarly, the FFS transition rates agree with those computed by the BF method, with the FFS method providing measurable and realistic transition rates at  $\tau = 0.53$  min, as well as low computational costs, showing the power of the FFS method for truly rare events. Figure 8 shows the variation of the local interface probabilities at  $\lambda_i$ , as interface temperatures vary, as an illustration, for  $\tau = 0.5$  min. While the local interface probabilities vary with the interface temperatures for every simulation run, the overall probabilities of transition; i.e., the products of the individual interface probabilities, do not change significantly.

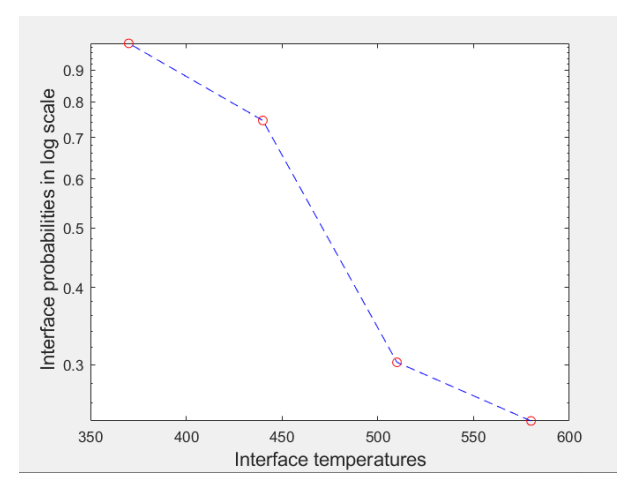


Figure 8. Probability of transition across  $\lambda_i$  as a function of temperature at  $\lambda_i$  for  $\tau = 0.5$  min with  $\sigma_n^2 = 0.02$ 

Table 3 summarizes the results of the BF and FFS algorithms at  $\sigma_{\eta}^2 = 0.02$ , where it can be seen that the initial rate of transition,  $r_1$ , the overall probability of transition,  $p_{\text{overall}}$ , and the FFS overall transition rate,  $k^{\text{FFS}}$ , decrease as  $\tau$  increases, it becoming more difficult to transition out of basin A. Having computed the transition rates, a dimensionless activation energy barrier,  $E_a$ , can be expressed as:

$$k^{\text{FFS}} = k_{\text{o}} \exp(-E_{\text{a}}) \tag{19}$$

and,

$$E_{\rm a} = -ln\left(\frac{k^{\rm FFS}}{k_{\rm o}}\right) \tag{20}$$

where  $k_0$  is a pre-exponential factor. Figure 9 shows the natural logs of  $k^{\text{FFS}}$  and  $k^{\text{BF}}$  as functions of the residence time,  $\tau$ , where it can be seen that both  $\ln(k^{\text{FFS}})$  and  $\ln(k^{\text{BF}})$  decrease linearly with  $\tau$ . Hence, given the decreasing dependence of  $k^{\text{FFS}}$  on  $\tau$ , and from Eq. (19), it can be concluded that  $E_a$  has an increasing dependence on  $\tau$ .

τ, min	$r_1$ , min <sup>-1</sup>	$p_{ m overall}$	k <sup>FFS</sup> , min <sup>-1</sup>	k <sup>BF</sup> , min⁻¹
0.5	6.12E-02	5.46E-02	3.34E-03	2.81E-03
0.51	2.95E-02	2.79E-02	8.23E-04	8.01E-04
0.52	2.00E-02	9.51E-03	1.90E-04	2.07E-04
0.53	8.91E-03	3.37E-03	3.00E-05	-

Table 3. Summary of Results for the Uncontrolled Process at  $\sigma_{\eta}^2 = 0.02$ 

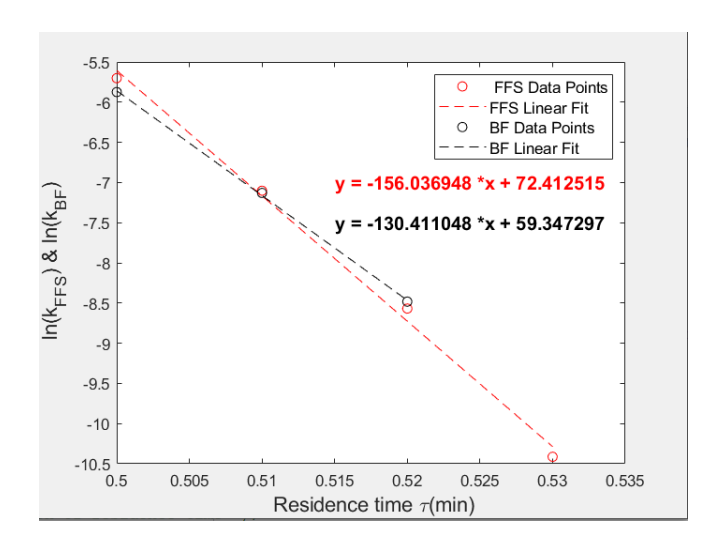


Figure 9. Natural log of FFS and BF rates of transition as functions of the residence time,  $\tau$ 

### 5.1.2. Residence Time Fixed at $\tau = 0.53$ min, Vary $\sigma_n^2$

At  $\tau$  = 0.53 min, the noise variance is increased over  $\sigma_{\eta}^2$  = 0.04-0.2. And, at lower noise variances; i.e.,  $\sigma_{\eta}^2$  < 0.1, the BF algorithm is carried out using multiple trajectories. In these cases, forward A-B transition rates,  $k_{\rm f}$ , are computed, as are backward B-A transition rates,  $k_{\rm b}$ , yielding an equilibrium constant:

$$K = \frac{k_{\rm f}}{k_{\rm h}} \tag{21}$$

However, for higher noise variances,  $\sigma_{\eta}^{2} \ge 0.1$ , the BF algorithm yields single long trajectories consisting of multiple back-and-forth, inter-basin transitions. Figure 10 shows the average survival probabilities; i.e.,  $p_{\rm A}(t)$  and  $p_{\rm B}(t)$ , at  $\tau=0.53$  min and  $\sigma_{\eta}^{2}=0.2$ , computed using the BF method.

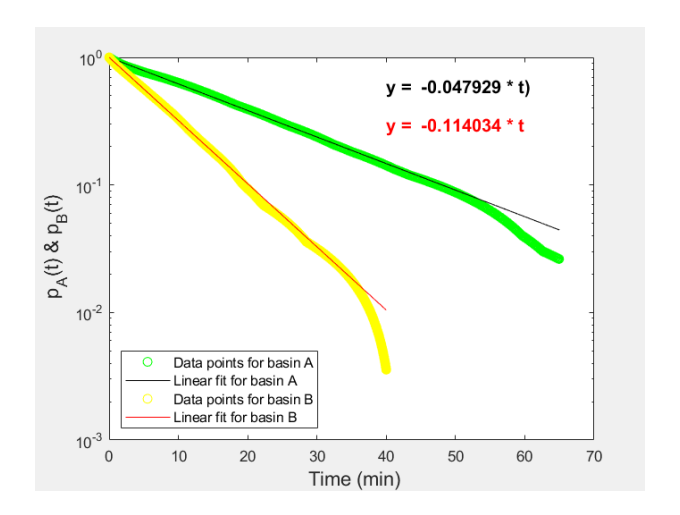
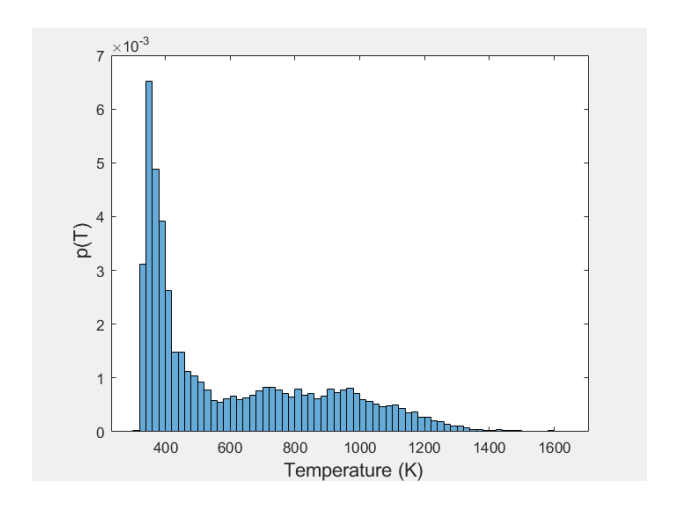


Figure 10. Survival probabilities for basins A,  $p_{\rm A}(t)$ , and B,  $p_{\rm B}(t)$ , as functions of time at  $\tau=0.53$  min and  ${\sigma_\eta}^2=0.2$ , computed using BF method

To further analyze trajectories with inter-basin, back-and-forth transitions, Figure 11 shows the probability at different temperatures, p(T), for the single trajectory at  $\tau = 0.53$  min and  $\sigma_{\eta}^2 = 0.2$ . Also, Figure 12 shows -ln (p(T)); that is, the Gibbs free-energy landscape of the process, where the two minima represent the most probable temperatures in the A and B basins.



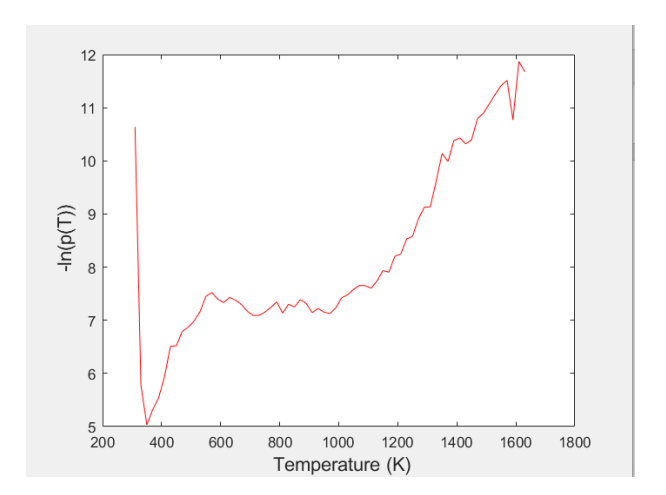
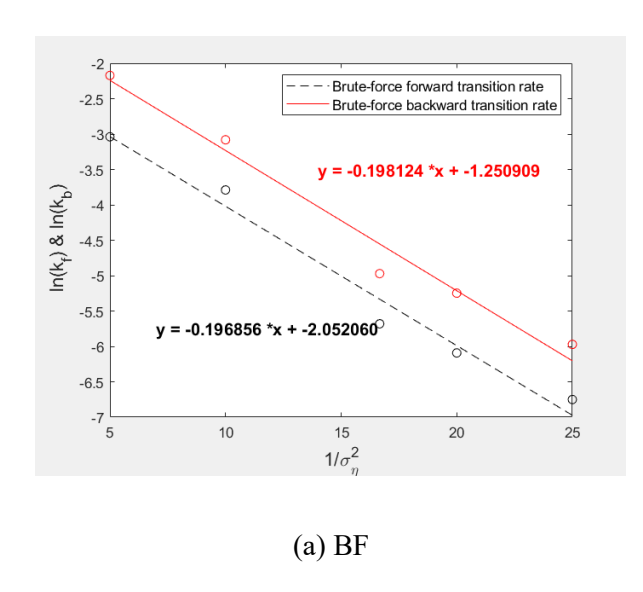


Figure 11. Probability p(T);  $\tau = 0.53$  min and  $\sigma_{\eta}^2 = 0.2$ 

Figure 12. -ln p(T);  $\tau = 0.53$  min and  $\sigma_{\eta}^{2} = 0.2$ 

Figures 13a,b show  $\ln{(k_{\rm f})}$  and  $\ln{(k_{\rm b})}$  as linearly decreasing functions of the reciprocal of noise variance,  $1/\sigma_{\eta}^{\ 2}$ , generated by BF and FFS analyses. Both the forward and backward transition rates increase with  $\sigma_{\eta}^{\ 2}$ , as expected, due to the increased instability. Figure 14 shows the weak dependence of the equilibrium constant, K, on  $\sigma_{\eta}^{\ 2}$ , for both BF and FFS methods, where it can be seen that K remains fairly constant in the range of 0.4-0.5 regardless of the value of  $\sigma_{\eta}^{\ 2}$ . Note that the transition rates and the equilibrium constant, K, computed by the BF method agree fairly with those computed by the FFS method. Also, at  $\tau = 0.53$  min and  $\sigma_{\eta}^{\ 2} = 0.03$ , FFS was able to compute transition rates for this truly rare transition, which could not be computed by the BF method, due to excessive computational cost.



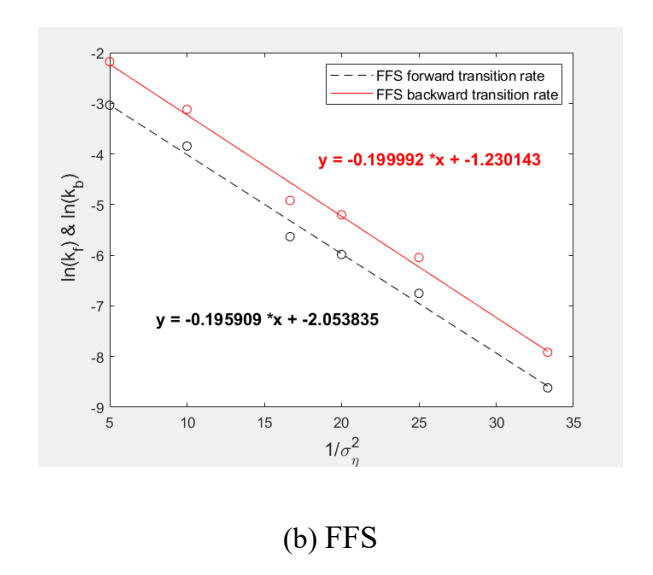


Figure 13.  $\ln{(k_{\rm f})}$  and  $\ln{(k_{\rm b})}$  as functions of  $^{1}/_{\sigma_{\eta}^{2}}$  for BF and FFS methods at  $\tau = 0.53$  min

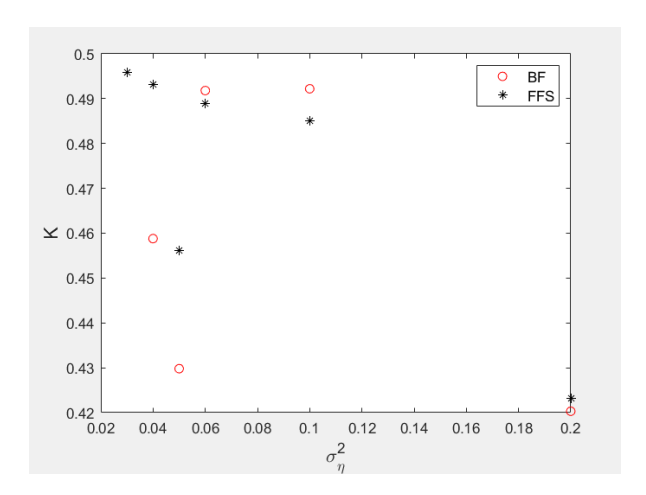


Figure 14. The weak dependence of the equilibrium constant, K, on the noise variance,  $\sigma_{\eta}^{2}$ , for both BF and FFS methods.

Next, it is possible to quantify approximately the experimental dependence of the equilibrium constant K on the noise variance,  $\sigma_{\eta}^2$ . The latter can be thought to add thermal effects to the process. Note that the following equations are proposals validated by our data and need not be true for any process, in general. Therefore, in accordance with statistical mechanics,  $\sigma_{\eta}^2$  can be described as:

$$\sigma_n^2 \propto RT_n \text{ or } \sigma_n^2 = cRT_n$$
 (22)

where R is the universal gas constant,  $T_{\eta}$  is the absolute temperature, and c is a proportionality constant. The forward and backward transition rates; i.e.,  $k_f$  and  $k_b$ , can be quantified using the Arrhenius equation:

$$k_{\rm f} = k_{\rm o,f} \exp(-E_{\rm f}/RT_{\eta})$$
  
 $k_{\rm b} = k_{\rm o,b} \exp(-E_{\rm b}/RT_{\eta})$  (23)

Therefore, the equilibrium constant, K, can be expressed as:

$$K = \frac{k_{\rm f}}{k_{\rm b}} = \frac{k_{\rm o,f}}{k_{\rm o,b}} \exp\left(-\frac{(E_{\rm f} - E_{\rm b})}{RT_{\eta}}\right) \tag{24}$$

where  $k_{\rm o,f}$  and  $k_{\rm o,b}$  are the forward and backward pre-exponential factors, and  $E_{\rm f}$  and  $E_{\rm b}$  are the forward and backward activation energies. The difference between the forward and backward activation energies; i.e.,  $E_{\rm f}-E_{\rm b}=\Delta G$ . Next, substituting  $RT_{\eta}$  from Eq. (22) into Eq. (24):

$$K = \frac{k_{\rm f}}{k_{\rm b}} = \frac{k_{\rm o,f}}{k_{\rm o,b}} \exp\left(-\frac{c\Delta G}{\sigma_{\eta}^2}\right) \tag{25}$$

The slope and intercept are used to compute the forward and backward pre-exponential factors; i.e.,  $k_{0,f}$  and  $k_{0,b}$ , and the forward and backward activation energies,  $E_f$  and  $E_b$ . Note that the linear equations © 2021. This manuscript version is made available under the CC-BY-NC-ND 4.0 license https://creativecommons.org/licenses/by-nc-nd/4.0/

obtained from the BF and FFS methods are sufficiently close for both the forward and backward transitions. These equations are equivalent to the natural log of Eq. (23), and consequently, yield  $k_{o,f}$  and  $k_{o,b}$ . Then, the difference between the slopes of  $\ln(k_f)$  and  $\ln(k_b)$ , provides  $E_f - E_b = \Delta G$ .

Table 4 below shows the quantitative parameters computed using the linear equations of  $\ln(k_{\rm f})$  and  $\ln(k_{\rm b})$  as functions of  $1/\sigma_{\eta}^2$ . It can be observed that  $\Delta G$  is negative and of smaller magnitudes,  $\sim O(10^{-3})$ . Also, for both the BF and FFS methods, the ratio of the pre-exponentials, i.e.,  $k_{\rm o,f}/k_{\rm o,b}$  is similar to the K values seen previously in Figure 14; i.e., in the range of 0.4-0.5. Hence, as observed previously in Figure 14, the equilibrium constant is a very weak function of the noise variance,  $\sigma_{\eta}^2$ , and strongly depends on the ratio of the forward and backward pre-exponential factors; i.e.,  $k_{\rm o,f}/k_{\rm o,b}$ .

Table 4. Computed Parameters from  $\ln{(k_{\rm f})}$  and  $\ln{(k_{\rm b})}$  as Functions of 1/  $\sigma_{\eta}^2$  at  $\tau = 0.53$  min

Method	$k_{ m o,f}$	$k_{ m o,b}$	$k_{ m o,f}/k_{ m o,b}$	$E_{\mathrm{f}}$	<b>E</b> <sub>b</sub>	ΔG
BF	0.1285	0.2862	0.449	0.1969	0.1981	-1.2E-03
FFS	0.1282	0.2922	0.4387	0.1959	0.2	-1.87E-03

### 5.2. Process Analysis with P-Control

# 5.2.1. Noise Variance Fixed at $\sigma_{\eta}^{\ 2}$ = 0.02, Vary $\tau$

In the first class of data-sets, the analyses of the forward A-B transitions by the BF and FFS algorithms are employed as described at fixed  $\sigma_{\eta}^{\ 2}=0.02$ , with  $\tau$  varied from 0.5-0.53 min, and considering  $K_{\rm C}=0.02$ , 0.05 and 0.1. Note that for the high control action at  $K_{\rm C}=0.1$ , in the FFS algorithm, the probability of transitioning from  $\lambda_3=440$  K to  $\lambda_4=370$  K was computed to be zero at all residence times. Also, note that the last order parameter was moved to 390 K (from 370 K) since below this temperature, the transition probabilities were computed to be zero. Hence, to conduct FFS analysis, the order parameters were further discretized between 440 and 390 K: (i)  $\lambda_0=650$  K, (ii)  $\lambda_1=580$  K, (iii)  $\lambda_2=510$  K, (iv)  $\lambda_3=440$  K, (v)  $\lambda_4=420$  K, (vi)  $\lambda_5=400$  K, (vii)  $\lambda_6=390$  K.

Figure 15 shows  $\ln (k^{FFS})$  as a function of the residence time without control and for three controller gains,  $K_C$ . The overall rates of transition decrease with increased residence time,  $\tau$ , at constant  $K_C$ , as the stability of the process in basin A increases. Also, the magnitude of the slope and intercept is highest for  $K_C = 0.1$ , as the high control action makes it harder for the process to transition out of the A basin. Figure 16 shows  $\ln (k^{FFS})$  as a function of the controller gain,  $K_C$ , for the four residence times, where non-linear decreasing behaviors for all four residence times can be observed. At constant  $\tau$ , the overall transition rates decrease with increased  $K_C$ , also due to increased stabilization of the process in basin A. This decrease is observed to be more prominent at  $K_C = 0.1$ , due to the high control action. Note that

the FFS algorithm computes transition rates at  $\tau = 0.53$  min and  $K_C = 0.1$ , truly rare transitions, considering the high stability of the process in basin A. But, as for the process without control, the BF analysis is unable to track them due to excessive computational costs.

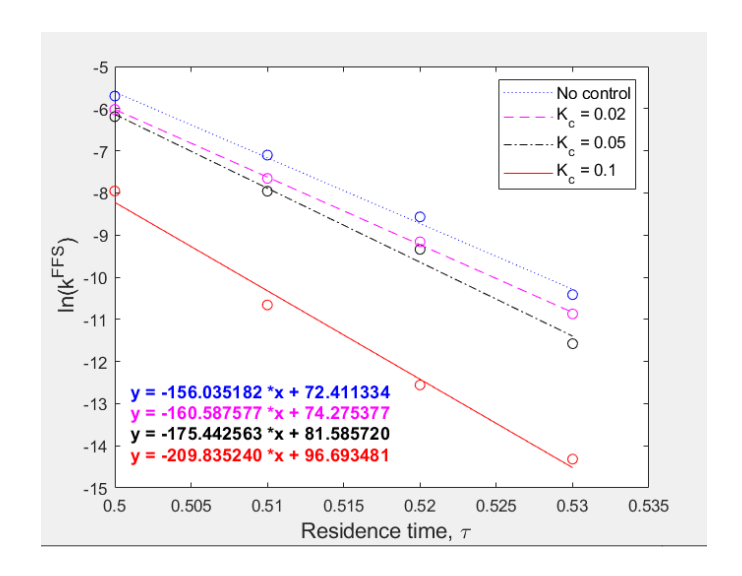


Figure 15.  $\ln{(k^{\text{FFS}})}$  as a function of the residence time,  $\tau$ , as the controller gain,  $K_{\text{C}}$ , varies, for  $\sigma_{\eta}^{\ 2} = 0.02$  using the FFS method

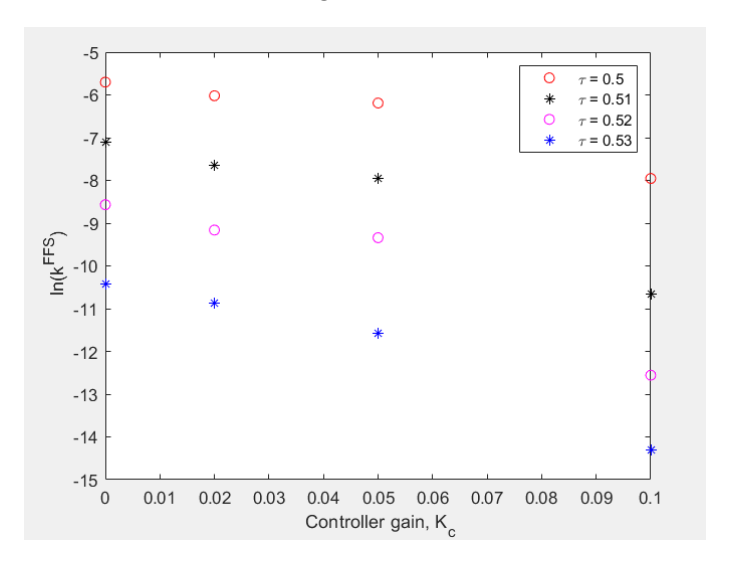


Figure 16.  $\ln{(k^{\rm FFS})}$  as a function of the controller gain,  $K_{\rm C}$ , as residence time,  $\tau$ , varies, for  ${\sigma_{\eta}}^2=0.02$  using the FFS method

# 5.2.2. Residence Time Fixed at $\tau = 0.53$ min, Vary $\sigma_{\eta}^{2}$

For the P-controlled process with  $\tau$  fixed at 0.53 min, analysis by the BF algorithm, as previously conducted for the uncontrolled process, is carried out using multiple trajectories when  $\sigma_{\eta}^{\ 2} < 0.1$ , and a © 2021. This manuscript version is made available under the CC-BY-NC-ND 4.0 license https://creativecommons.org/licenses/by-nc-nd/4.0/

long, single trajectory with multiple back-and-forth inter-basin transitions when  $\sigma_{\eta}^{\ 2} \ge 0.1$ . Similarly, for the FFS method, the last basin between 440 K and 390 K is further discretized when  $K_{\rm C}=0.1$ . Figure 17 shows the decreasing trends for  $\ln{(k_{\rm f})}$  and  $\ln{(k_{\rm b})}$  as functions of  $1/\sigma_{\eta}^{\ 2}$  for the FFS method, for  $K_{\rm c}=0.02$  and 0.05. Figures 18a,b shows the non-linear dependence of  $\ln{(k_{\rm f})}$  and  $\ln{(k_{\rm b})}$  on the controller gain,  $K_{\rm c}$ , for fixed  $\sigma_{\eta}^{\ 2}$ , where it can be observed that the forward transition rates,  $k_{\rm f}^{\rm FFS}$ , decrease with increasing  $K_{\rm C}$ , as the increased control action increases the stability of the process in basin A. On the other hand, the backward transition rates,  $k_{\rm b}^{\rm FFS}$ , increase with increasing  $K_{\rm C}$ , as the increased control action decreases the stability of the process in basin B. Additionally, it can be observed that at  $K_{\rm c}=0.1$ ,  $\ln{(k_{\rm b}^{\rm FFS})}$  appear close to one another for all  $\sigma_{\eta}^{\ 2}$ .

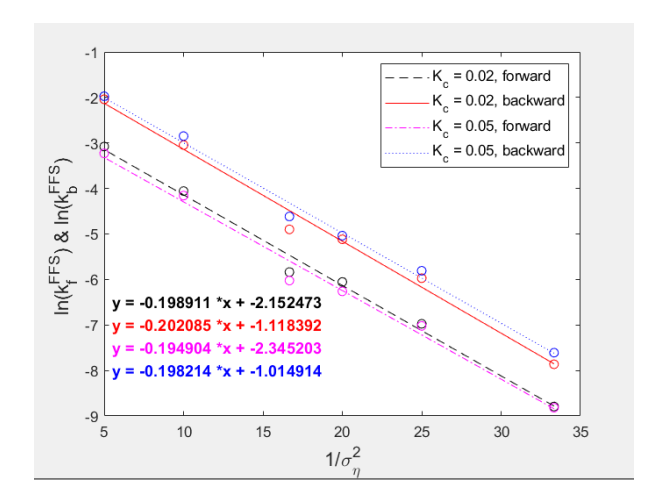


Figure 17.  $\ln (k_{\rm f})$  and  $\ln (k_{\rm b})$  as functions of  $1/\sigma_{\eta}^2$  for the FFS method for  $K_{\rm c}=0.02$  and 0.05

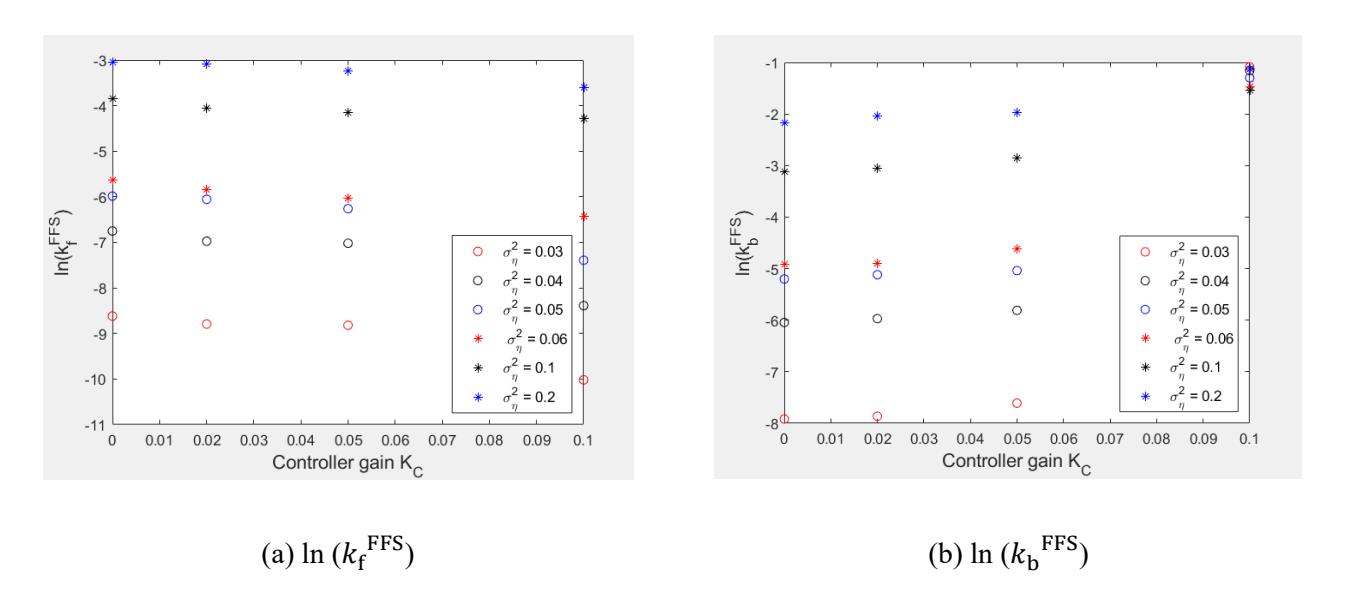


Figure 18.  $\ln{(k_{\rm f}^{\rm FFS})}$  and  $\ln{(k_{\rm b}^{\rm FFS})}$  as functions of the controller gain,  $K_{\rm C}$ , for fixed  $\sigma_{\eta}^{2}$ 

Figure 19 shows the weak dependence of K on  $\sigma_{\eta}^2$  for the uncontrolled and two P-controlled configurations. Consequently, K decreases with increasing control action. Note that, as without control, the BF method does not compute the transition rates at  $K_{\rm C}=0.1$  due to excessive computational costs. In contrast to prior observations, at  $K_{\rm C}=0.1$ , Figure 20 shows the strong linear dependence of  $\ln(K)$  on  $1/\sigma_{\eta}^2$ . In this case, as seen in Figure 21,  $k_{\rm f}^{\rm FFS}$  increases significantly with  $\sigma_{\eta}^2$ , but  $k_{\rm b}^{\rm FFS}$  does not change significantly because the added control action, at  $K_{\rm C}=0.1$ , does not significantly increase the instability of the B basin – thus causing K to change significantly with  $\sigma_{\eta}^2$ . At such high control action, the process is already very unstable in the B basin – hence, increases in  $\sigma_{\eta}^2$  do not affect  $k_{\rm b}^{\rm FFS}$  significantly.

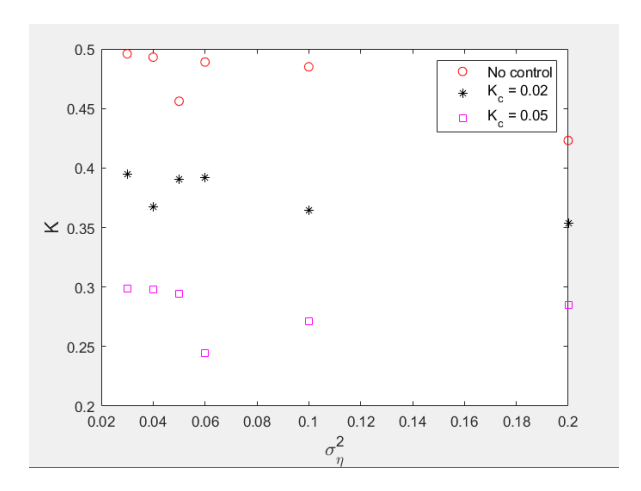
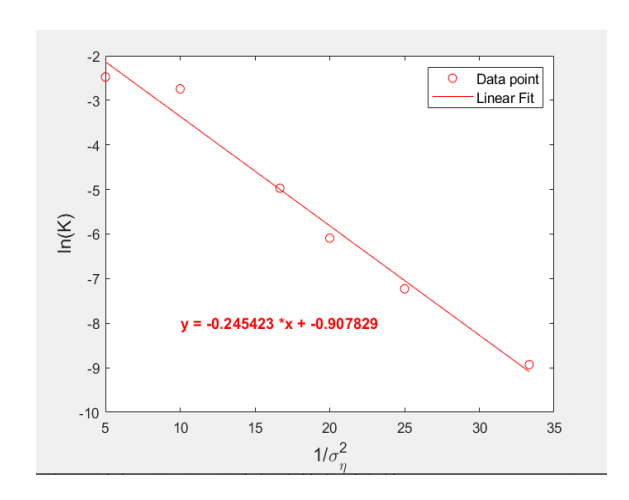


Figure 19. K as a weak function of  $\sigma_{\eta}^{\ 2}$  for the three process configurations



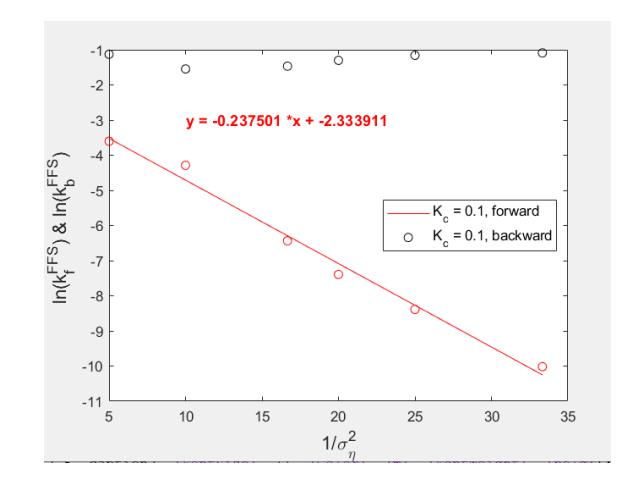


Figure 20. ln (*K*) as a function of  $1/\sigma_{\eta}^2$  for  $K_C = 0.1$ 

Figure 21.  $\ln{(k_{\rm f}^{\rm FFS})}$  and  $\ln{(k_{\rm b}^{\rm FFS})}$  as functions of  $1/\sigma_{\eta}^{\rm 2}$  for  $K_{\rm C}=0.1$ 

As shown previously, the dependence of K on  $\sigma_{\eta}^2$  is quantified from plots of  $\ln{(k_{\rm f}^{\rm FFS})}$  and  $\ln{(k_{\rm b}^{\rm FFS})}$  as functions of  $1/\sigma_{\eta}^2$  in Figure 17. As seen in Figure 20, because K is a strong function of  $\sigma_{\eta}^2$  for © 2021. This manuscript version is made available under the CC-BY-NC-ND 4.0 license https://creativecommons.org/licenses/by-nc-nd/4.0/

 $K_{\rm C}=0.1$ , the linear equation quantitatively relates K and  $\sigma_{\eta}^2$ , with the slope equaling  $c\Delta G$ , and the exponential of the intercept equaling  $k_{\rm o,f}/k_{\rm o,b}$ .

Table 5 shows the quantitative parameters computed using the linear equations for  $\ln{(k_{\rm f}^{\rm FFS})}$  and  $\ln{(k_{\rm b}^{\rm FFS})}$  as functions of  $1/\sigma_{\eta}^{\ 2}$ . For all cases except  $K_{\rm C}=0.1,\ k_{\rm o,f}/k_{\rm o,b}$  decreases with increasing control action, with  $k_{\rm o,f}/k_{\rm o,b}$  similar to the K values seen previously and the magnitude of the small, negative  $\Delta G$  ( $\sim O(10^{-3})$ ) increases with increasing control action. For  $K_{\rm C}=0.1,\ \Delta G$  is observed to be positive, with a much higher magnitude. Therefore, K is a very weak function of the noise variance,  $\sigma_{\eta}^{\ 2}$ , for all cases except for P-control with  $K_{\rm C}=0.1$ .

Table 5. Computed Parameters from  $\ln{(k_{\rm f})}$  and  $\ln{(k_{\rm b})}$  as Functions of  $1/\sigma_{\eta}^2$  at  $\tau = 0.53$  min for the P-controlled Process, Using FFS

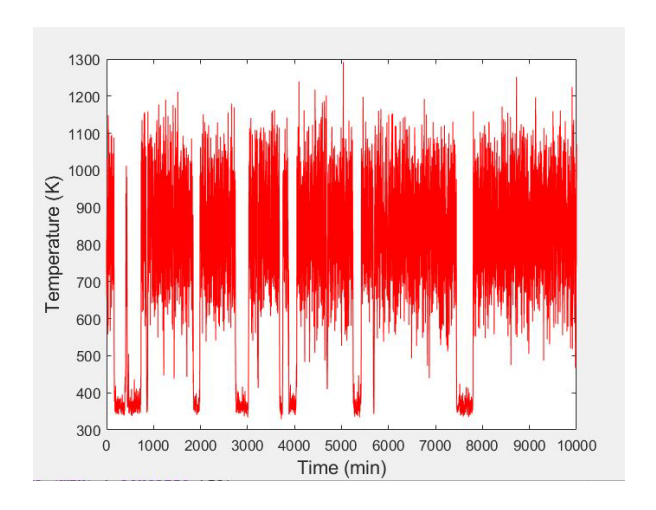
Kc	$k_{ m o,f}$	$k_{ m o,b}$	$k_{ m o,f}/k_{ m o,b}$	$\boldsymbol{E}_{\mathbf{f}}$	$E_{\mathrm{b}}$	ΔG
-	0.1282	0.2922	0.4387	0.1959	0.2	-1.87E-03
0.02	0.1162	0.3268	0.3556	0.1989	0.2021	-3.17E-03
0.05	0.0958	0.3624	0.2644	0.1949	0.1982	-3.3E-03
0.1	-	-	0.4034	-	-	+0.2454/c

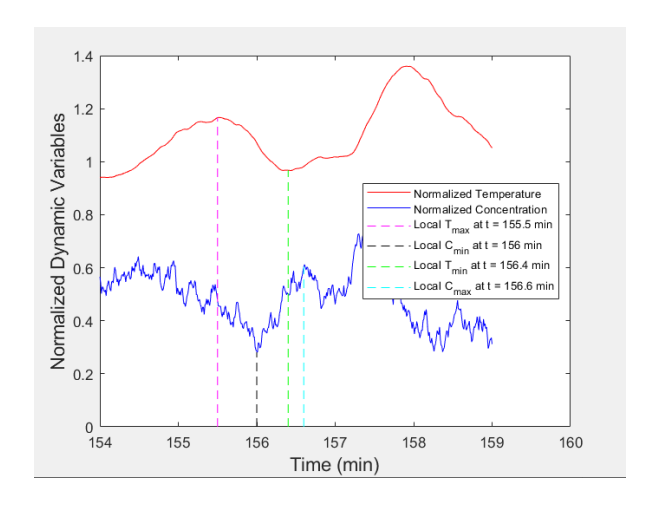
### 5.3. Dynamic Analyses Tracking Long Process Trajectories

To understand better the behavior of the long process trajectories, key process variables were examined as dynamic profiles proceeded in the vicinity of transitions from basin-to-basin. For  $\tau = 0.53$  min and  $\sigma_{\eta}^2 = 0.04$ , trajectories for uncontrolled and P-controlled processes, with  $K_C = 0.05$  and  $F_{C0} = 30$  m<sup>3</sup>/min, were studied. Figures 22a,b show the temperature profile and a magnified plot of the normalized temperature and concentration between t = 154 and 159 min, where the first forward transition is initiated. Note that the temperature, T, and the outlet concentration,  $C_A$ , are normalized using their high temperature-high conversion steady states; i.e., T/800 and  $C_A/1.05$ . It can be observed here that as  $C_A$ decreases, due to high conversion, T increases, and as  $C_A$  increases, due to low conversion, T decreases. Hence, increases/decreases in concentration,  $C_A$ , impacted more directly by concentration noise, lead to low and high peaks in temperature. The first temperature local maximum is observed at t = 155.5min, followed by the first local concentration minimum, observed at t = 156 min. This appears to indicate that the temperature changes first followed by a short lag in concentration. This can also be seen when the first local temperature minimum is observed at t = 156.4 min, followed by the first local concentration maximum at t = 156.6 min. To validate this observation, multiple long trajectories were initiated, with each trajectory consisting of finite back-and-forth inter-basin transitions, and for each © 2021. This manuscript version is made available under the CC-BY-NC-ND 4.0

license https://creativecommons.org/licenses/by-nc-nd/4.0/

transition region of every trajectory, the temperature appeared to lead the concentration. Because the noise is added directly to the concentration, it was expected that the concentration would lead the temperature – but because the temperature leads the concentration, the thermal effects brought by the noise, affect the temperature before the concentration, and thereby, cause the transition.



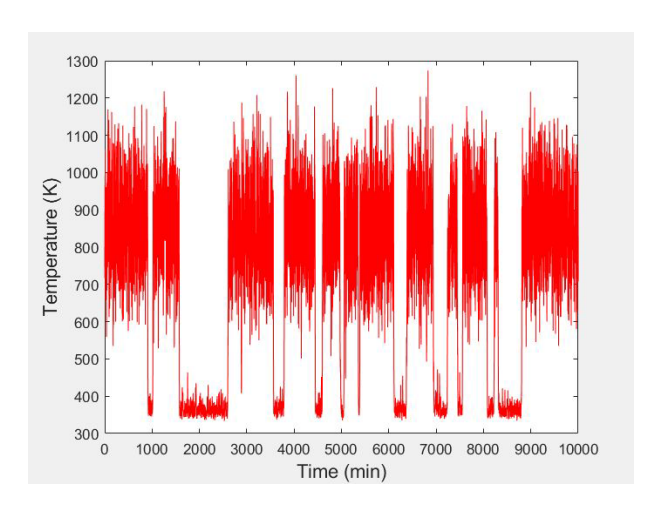


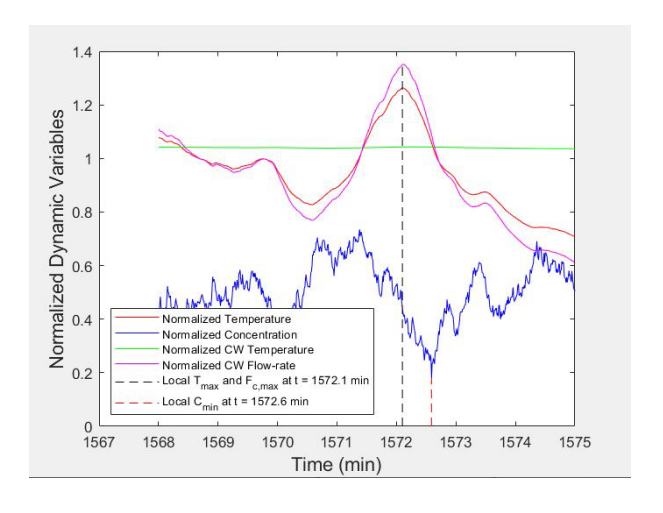
(a) Temperature profile

(b) Normalized dynamic variables, magnified from t = 154 to 159 min

Figure 22. Temperature profile and magnified plot of the normalized dynamic variables for the uncontrolled process at  $\tau = 0.53$  min and  $\sigma_{\eta}^{\ 2} = 0.04$ 

Figure 23a.b similarly show the temperature profile and the magnified plot of the normalized dynamic variables between t = 1568 and 1575 min for the P-controlled process with  $K_C = 0.05$  and  $F_{C0} = 30$  m<sup>3</sup>/min, with the two additional dynamic variables being the normalized cooling water (CW) temperature and normalized CW flow-rate, normalized respectively at their steady state values, i.e.,  $T_C/300$  and  $F_C/30$ . It can be observed that T continues to lead  $C_A$ , and  $T_C$  does not respond to changes in T and  $C_A$ .  $F_C$  responds almost immediately to the changes in the process temperature, T, with maximum and minimum peaks for each observed at nearly equal time instants.





(a) Temperature profile

(b) Normalized dynamic variables, magnified to t = 1568 and 1575 min

Figure 23. Temperature profile and magnified plot of the normalized dynamic variables for the P-controlled process at  $\tau = 0.53$  min,  $\sigma_{\eta}^2 = 0.04$ ,  $K_C = 0.05$  and  $F_{C0} = 30$  m<sup>3</sup>/min

### 5.4. Comparison with Transition-Path Sampling (TPS)

Rare-event analysis by FFS yields numerous benefits beyond TPS. First, TPS requires that an initial trajectory be generated that transitions between basins of normal operation and interlock activation. Then, additional trajectories are generated by random perturbations from the initial trajectory. But, these may require high computational costs, especially when transition probabilities are very small. Also, each new trajectory, from its perturbation point, must be integrated forward and backward over a pre-specified simulation time. Often, however, the trajectories are too similar to the initial trajectory. More significantly, the backward integrations often encounter numerical instability, requiring boundary-value optimization techniques such as the "shooting" (Bock et al., 2000) and orthogonal collocation (Cuthrell and Biegler, 1989) methods, adding to the computational costs. Also, because TPS does not generate trajectories in a piece-wise manner, it is difficult to use for rate or committer analysis, which is achieved easily using FFS.

To circumvent these disadvantages, by integrating solely forward from the initial basin to the final basin, FFS generates more independent rare paths – each having different time durations, while TPS rare paths have the same duration. This broader distribution of rare paths can lead to improved alarm systems, to be demonstrated in future research.

#### 6. Conclusions

The FFS method, in particular the DFFS variant, can simulate and detect rare-event transitions between normal and abnormal operating conditions resulting in automated plant shutdowns, which adversely impact plant reliability. It generates numerous rapid-transition trajectories, that occur rarely, sharply reducing their discovery time, as shown herein, from weeks to just a few minutes. Transitions away from normal operation are made either by adding noise directly to the operating parameters affecting multiple balance equations, called 'parametric noise', or by adding properly-scaled 'non-parametric' noise terms in single balance equations.

Hence, the stochastic nature of the FFS method and its ability to generate large numbers of rare-event trajectories have been demonstrated herein using a simple, dynamic exothermic CSTR model with non-parametric noise added to the inlet concentration. At increased noise variance,  $\sigma_{\eta}^{2}$ , the inter-basin back-and-forth transitions observed for not-so-rare events are noteworthy. Results generated by the FFS method are clearly more reliable than those by the BF method, achieved at lower computational costs — with the largest differences being for truly rare-events. While the weak dependence of K on  $\sigma_{\eta}^{2}$  at fixed  $\tau$  was anticipated (because increases in  $\sigma_{\eta}^{2}$  cause increases to both  $k_{\rm f}$  and  $k_{\rm b}$ ), the strong dependence of K on  $\sigma_{\eta}^{2}$  at high control action (i.e., at  $K_{\rm C} = 0.1$ ) was unanticipated.

Given the simplicity of the exothermic CSTR model, investigations of rare-event pathways for more rigorous CSTR models are justified. Also, applications of the FFS method to explore rare-events in complex large-scale processes, such as steam-methane reformers (SMRs) and air-separation units (ASUs) are justified. Note that, for the latter, transition-path sampling (TPS) was utilized to trace rare-event paths (Moskowitz et al., 2018).

### 7. Acronyms

Acronym	Term	
ASU	Air-separation Unit	
BF	Brute-force	
BG	Branched-growth	
CSTR	Continuous Stirred Tank Reactor	
DFFS	Direct Forward-Flux Sampling	
FFS	Forward-Flux Sampling	
MD	Molecular Dynamics	
MPS	Model-Predictive Safety	
PI	Proportional-Integral	
RB	Rosenbluth	
SIS	Safety Instrumented System	

SMR	Steam-Methane Reformer
TPS	Transition-Path Sampling

### 8. Nomenclature

# English

Variables	Quantity	Units
A	Heat Transfer Area	m <sup>2</sup>
$C_{ m A}$	Outlet concentration of Reactant A	kmol m <sup>-3</sup>
$C_{ m Af}$	Feed Concentration of Reactant A	kmol m <sup>-3</sup>
$C_{p}$	Specific Heat Capacity of Feed	kJ kg <sup>-1</sup> K <sup>-1</sup>
$C_{ m pw}$	Specific Heat Capacity of Water	kJ kg <sup>-1</sup> K <sup>-1</sup>
E	Activation Energy	kJ kmol <sup>-1</sup>
$\boldsymbol{\mathit{E}}_{\mathbf{a}}$	Dimensionless Activation Barrier	-
$E_{\mathbf{b}}$	Backward Activation Energy	kJ kmol <sup>-1</sup>
$E_{\mathrm{f}}$	Forward Activation Energy	kJ kmol <sup>-1</sup>
$e_I$	Integral Error	K min
F	Feed Flow-rate	kmol min <sup>-1</sup>
$F_{ m C}$	Cooling Water (CW) Flow-rate	m³ min-1
$F_{ m C0}$	Steady State CW Flow-rate	m³ min-1
$F_{ m Cmax}$	Maximum Saturated CW Flow-rate	m³ min-1
h	Integration Step-size	min
K	Equilibrium Constant	-
$K_{ m BF}$	Brute-force Equilibrium Constant	-
$K_{\mathrm{C}}$	Controller Gain	m <sup>3</sup> mol <sup>-1</sup> K <sup>-1</sup>
$K_{ t FFS}$	FFS Equilibrium Constant	-
$k^{ m BF}$	Brute-force Rate of Transition	min <sup>-1</sup>
$k^{ m FFS}$	FFS Rate of Transition	min <sup>-1</sup>
$k_{ m b}$ BF	BF Backward Transition Rate	min <sup>-1</sup>
$k_{ m f}{}^{ m BF}$	BF Backward Transition Rate	min <sup>-1</sup>
$k_{ m f}{}^{ m FFS}$	FFS Forward Transition Rate	min <sup>-1</sup>
$k_{ m b}$ FFS	FFS Backward Transition Rate	min <sup>-1</sup>
$k_{o,b}$	Backward Pre-exponential Factor	min <sup>-1</sup>
$k_{o,f}$	Forward Pre-exponential Factor	min <sup>-1</sup>
N	Number of Trajectories	-
$N_0$	Number of Initial Crossings	-

N <sub>interface</sub>	Number of Interfaces	-
$N_{t}$	Number of Intervals Beginning in Basin A	-
$n_{ m t}$	Number of Intervals Surviving in Basin A	-
p(T)	Probability at Different Temperatures	-
p(t)	Survival Probability	-
$p_{\rm A}({ m t})$	Survival Probability within A Basin	-
$p_{\mathrm{B}}(t)$	Survival Probability within B Basin	-
$p_{ m overall}$	Overall Probability of Transition	-
R	Universal Gas Constant	kJ kmol <sup>-1</sup> K <sup>-1</sup>
-r	Rate of Reaction	kmol m <sup>-3</sup> min <sup>-1</sup>
$r_1$	Initial Rate of Transition	min <sup>-1</sup>
T	Outlet Temperature	K
$T_{base}$	Base Temperature	K
$T_{ m c}$	CW Temperature	K
$T_{\mathrm{C0}}$	Inlet CW Temperature	K
$T_{ m Cmax}$	Maximum Saturated CW Temperature	K
$T_{ m f}$	Feed Temperature	K
$T_{ m SP}$	Set-point Temperature	K
$T_{\eta}$	Absolute Temperature	K
t	Time Variable	min
$t_0$	Initial Time	min
$t_{ m AB}$	Transition Time	min
$t_{ m sim}$	Simulation Duration of Trajectory	min
$ar{t}_A$	Survival Time in A Basin	min
U	Overall Heat Transfer Coefficient	kJ min <sup>-1</sup> K <sup>-1</sup> m <sup>-2</sup>
V	Reactor Volume	$m^3$
$V_{ m j}$	Jacket Volume	$\mathrm{m}^3$

## Greek

Variables	Quantity	Units
$\Delta G$	Change in Gibbs Free Energy	kJ kmol <sup>-1</sup>
$\Delta H$	Heat of Reaction	kJ kmol <sup>-1</sup>
η	Noise	kmol m <sup>-3</sup>
λ	Order Parameter	K
$\mu$	Mean	kmol m <sup>-3</sup>

ρ	Feed Density	kg m <sup>-3</sup>
$ ho_{\scriptscriptstyle  m W}$	Water Density	kg m <sup>-3</sup>
$\sigma_{ m T}$	Standard Deviation	K
${\sigma_{\eta}}^2$	Noise Variance	kmol <sup>2</sup> m <sup>-6</sup>
τ	Residence Time	min
$ au_{ m c}$	Transition Time Constant	min <sup>-1</sup>
$ au_I$	Integral Time Constant	min

#### 9. References

- Allen, R.J., Frenkel, D., ten Wolde, P.R., 2006. Simulating rare events in equilibrium or nonequilibrium stochastic systems. Journal of Chemical Physics. https://doi.org/10.1063/1.2140273
- Allen, R.J., Valeriani, C., Rein Ten Wolde, P., 2009. Forward flux sampling for rare event simulations. Journal of Physics Condensed Matter 21. https://doi.org/10.1088/0953-8984/21/46/463102
- Bi, Y., Li, T., 2014. Probing methane hydrate nucleation through the forward flux sampling method, in: Journal of Physical Chemistry B. https://doi.org/10.1021/jp503000u
- Bock, H.G., Diehl, M.M., Leineweber, D.B., Schlöder, J.P., 2000. A Direct Multiple Shooting Method for Real-Time Optimization of Nonlinear DAE Processes, in: Nonlinear Model Predictive Control. https://doi.org/10.1007/978-3-0348-8407-5 14
- Bolhuis, P.G., Chandler, D., Dellago, C., Geissler, P.L., 2002. Throwing Ropes Over Rough Mountain Passes, in the Dark. Annual Review of Physical Chemistry 53. https://doi.org/10.1146/annurev.physchem.53.082301.113146
- Cuthrell, J.E., Biegler, L.T., 1989. Simultaneous optimization and solution methods for batch reactor control profiles. Computers and Chemical Engineering 13. https://doi.org/10.1016/0098-1354(89)89006-4
- Filion, L., Hermes, M., Ni, R., Dijkstra, M., 2010. Crystal nucleation of hard spheres using molecular dynamics, umbrella sampling, and forward flux sampling: A comparison of simulation techniques. Journal of Chemical Physics. https://doi.org/10.1063/1.3506838
- Horsch, M., Vrabec, J., Bernreuther, M., Grottel, S., Reina, G., Wix, A., Schaber, K., Hasse, H., 2008. Homogeneous nucleation in supersaturated vapors of methane, ethane, and carbon dioxide predicted by brute force molecular dynamics. Journal of Chemical Physics 128. https://doi.org/10.1063/1.2907849
- Jiang, H., Haji-Akbari, A., Debenedetti, P.G., Panagiotopoulos, A.Z., 2018. Forward flux sampling calculation of homogeneous nucleation rates from aqueous NaCl solutions. Journal of Chemical Physics 148. https://doi.org/10.1063/1.5016554
- Mehta, B.R., Reddy, Y.J., 2015. Alarm management systems, in: Industrial Process Automation Systems. https://doi.org/10.1016/b978-0-12-800939-0.00021-8

- Moskowitz, I.H., Seider, W.D., Patel, A.J., Arbogast, J.E., Oktem, U.G., 2018. Understanding rare safety and reliability events using transition path sampling. Computers and Chemical Engineering. https://doi.org/10.1016/j.compchemeng.2017.06.016
- Muñoz, M.A., Grinstein, G., Tu, Y., 1997. Survival probability and field theory in systems with absorbing states. Physical Review E Statistical Physics, Plasmas, Fluids, and Related Interdisciplinary Topics 56. https://doi.org/10.1103/PhysRevE.56.5101
- Yeh, I.C., Hummer, G., 2002. Peptide loop-closure kinetics from microsecond molecular dynamics simulations in explicit solvent. Journal of the American Chemical Society 124. https://doi.org/10.1021/ja025789n
- Zhang, Y., McCammon, J.A., 2003. Studying the affinity and kinetics of molecular association with molecular-dynamics simulation. Journal of Chemical Physics 118. https://doi.org/10.1063/1.1530162

### 10. Acknowledgments

The NSF CBET funding for our EAGER GOALI grant, 1839535, is greatly appreciated. Also, the suggestions and advice of Dr. Ian Moskowitz, Prof. Masoud Soroush, and Dr. Ulku Oktem were very helpful. The initial descriptions by Nick Baylis were also helpful and very much appreciated.